HHS Public Access

Author manuscript

Nat Med. Author manuscript; available in PMC 2016 September 21.

Published in final edited form as:

Nat Med. 2016 April ; 22(4): 388–396. doi:10.1038/nm.4067.

Modeling Smith-Lemli-Opitz syndrome with iPS cells reveals a causal role for Wnt/β-catenin defects in neuronal cholesterol synthesis phenotypes

Kevin R. Francis[1,2,*], **Amy N. Ton**[1], **Yao Xin**[3], **Peter E. O'Halloran**[1], **Christopher A. Wassif**[2], **Nasir Malik**[1], **Ian M. Williams**[2], **Celine V. Cluzeau**[2], **Niraj S. Trivedi**[4], **William J. Pavan**[5], **Wonhwa Cho**[3], **Heiner Westphal**[1], and **Forbes D. Porter**[2,*]

[1]Program in Genomics of Differentiation, The *Eunice Kennedy Shriver* National Institute of Child Health and Human Development, NIH; Bethesda, MD, USA

[2]Program in Developmental Endocrinology and Genetics, The *Eunice Kennedy Shriver* National Institute of Child Health and Human Development, NIH; Bethesda, MD, USA

[3]Department of Chemistry, University of Illinois at Chicago, Chicago, IL, USA

[4]Computational and Statistical Genomics Branch; National Human Genome Research Institute, NIH, Bethesda, MD, USA

[5]Genetic Diseases Research Branch; National Human Genome Research Institute, NIH, Bethesda, MD, USA

Abstract

Smith-Lemli-Opitz syndrome (SLOS) is a malformation disorder caused by mutations in *DHCR7*, impairing the reduction of 7-dehydrocholesterol to cholesterol. SLOS results in cognitive impairment, behavioral abnormalities, and nervous system defects, though neither cellular targets nor affected signaling pathways are defined. Whether 7-dehydrocholesterol accumulation or cholesterol loss is primarily responsible for disease pathogenesis is also unclear. Using induced pluripotent stem cells (iPSCs) from SLOS subjects, we identified cellular defects leading to precocious neuronal specification within SLOS derived neural progenitors. We also demonstrated that 7-dehydrocholesterol accumulation, not cholesterol deficiency, is critical for SLOS-associated defects. We further identified downregulation of Wnt/β-catenin signaling as a key initiator of

*Correspondence: ; Email: kevin.francis@sanfordhealth.org (K.R.F.); phone: 605-312-6422; fax: 605-328-0401. ; Email: fdporter@mail.nih.gov (F.D.P.); phone: 301-435-4432; fax: 301-480-5791

Accession Numbers

The microarray data are available in the Gene Expression Omnibus (GEO) database (http://www.ncbi.nlm.nih.gov/gds) under the accession number *GSE61203*.

Competing financial interests

The authors declare no competing financial interests.

Author contributions

K.R.F. and F.D.P. designed and directed the study, analyzed data, and wrote the manuscript. K.R.F., A.N.T., P.E.O., N.M., I.M.W., C.V.C. performed experiments and analyzed data. H.W. contributed to study design. C.A.W. provided assistance with GC/MS and study design. N.S.T. and W.J.P. provided support and performed statistical analysis of microarray experiments. Y.X. and W.C. designed, carried out, and analyzed experiments on lipid-protein interactions.

aberrant SLOS iPSCs differentiation through the direct inhibitory effects of 7-dehydrocholesterol on the formation of an active Wnt receptor complex. Activation of canonical Wnt signaling prevented the neural phenotypes observed in SLOS iPSCs, suggesting that Wnt signaling may be a promising therapeutic target for SLOS.

Introduction

Impaired cholesterol synthesis underlies a group of human disorders characterized by cognitive impairment, congenital malformations, and distinct behavioral phenotypes, including autism[1]. The most common cholesterol synthesis disorder, Smith-Lemli-Opitz syndrome (SLOS), results from mutations in 3β-hydroxysterol-Δ^7-reductase gene (*DHCR7*). Impaired DHCR7 activity inhibits the reduction of 7-dehydrocholesterol (7DHC) to cholesterol, resulting in lower cholesterol and higher 7DHC levels[2]. Cholesterol participates in multiple biological functions in the context of neurodevelopment and normal neuronal function, including synaptic activity, signal transduction, myelination, and as a precursor for neuroactive steroids[3–6]. While the cholesterol synthesis defect in SLOS may underlie pathological changes in multiple tissues, neurocognitive manifestations remain a major clinical issue. However, the precise effects of altering sterol composition on central nervous system (CNS) malformations, as well as cognitive and behavioral deficits found in SLOS patients, are unknown[7,8]. Furthermore, it is unclear whether the SLOS phenotype is a result of cholesterol deficiency or the effects of 7DHC accumulation[9,10]. Thus, while the SLOS biochemical defect is well defined, neither the specific mechanisms nor the role of decreased cholesterol versus increased 7DHC in SLOS CNS pathogenesis have been clearly delineated[1].

Results

Development of an iPSC model of SLOS

To gain insight into the mechanisms underlying neural phenotypes of SLOS, we generated induced pluripotent stem cells (iPSCs) via lentiviral transduction with the LoxP flanked STEMCCA polycistronic vector[11]. Fibroblasts from five SLOS subjects were selected to obtain iPSCs representative of the SLOS phenotypic spectrum (Supplementary Table 1). We generated and analyzed ≥2 lines corresponding to each SLOS subject to limit heterogeneity[12]. No significant differences in reprogramming efficiency were found between control and SLOS samples.

When cultured in cholesterol replete medium, both SLOS and control iPSCs exhibited typical human embryonic stem cell (hESC) morphology and high expression of pluripotent surface markers and core transcription factors relative to hESCs (Fig. 1a–c, Supplementary Fig. 1a–c, Supplementary Table 2). All iPSCs used in this study were karyotypically normal over > 30 passages, demonstrated silencing of viral reprogramming factors, and maintained patient-specific *DHCR7* mutations (Supplementary Fig. 1d–f). To confirm the differentiation capacity of iPSCs, we performed *in vitro* and *in vivo* germ layer differentiation assays. Analysis of differentiated iPSCs at the transcriptional, protein, and histological levels

demonstrated that SLOS and control iPSCs contribute to all three germ layers (Fig. 1d, Supplementary Fig. 2, and Supplementary Movie 1).

In order to induce cholesterol synthesis and cause 7DHC accumulation in SLOS lines, iPSCs were transferred from cholesterol replete hESC media to cholesterol deficient mTeSR1 media[13]. We confirmed that mTeSR1 medium was cholesterol deficient by gas chromatography/mass spectroscopy analysis (GC/MS) (0.33 ± 0.15 mcg cholesterol/mL in mTeSR1 vs. 9.83 ± 0.40 mcg cholesterol/mL in 20% KOSR hESC media). As expected, hESCs and control iPSCs did not accumulate either 7DHC or 8-dehydrocholesterol (8DHC; an isomer of 7DHC), and maintained normal cholesterol levels in both cholesterol replete and deficient medium. In contrast, SLOS iPSCs cultured in cholesterol deficient mTeSR1 medium demonstrate lower cholesterol levels and higher 7DHC and 8DHC levels compared to hESC and iPSC controls (Fig. 1e–h). These experiments validate the pluripotent capacity of SLOS iPSCs and confirm retention of the expected biochemical defect.

DHCR7 mutations result in stem cell defects and aberrant neural differentiation

We have previously identified increased dendritic and axonal growth in hippocampal neurons derived from *Dhcr7*$^{-/-}$ mice[14] and characterized structural abnormalities, including cerebral and cerebellar atrophy, in the CNS of SLOS subjects[7], suggesting that *DHCR7* mutations may affect neural development. The generation of neural rosettes, representing early neural progenitors of the developing CNS, is a standard assay for neural progenitor derivation[15]. To analyze SLOS iPSC neural progenitors, neurospheres were generated in cholesterol replete medium and plated onto laminin-coated dishes in cholesterol deficient neural induction media. While hESCs and control iPSCs demonstrated robust formation of SOX2/PAX6 positive rosettes (Fig. 2a), SLOS iPSC-generated SOX2/PAX6 positive rosette structures were poorly defined and displayed accelerated neuronal differentiation, as evidenced by higher expression of the neuronal marker βIII-tubulin compared to ES/iPSC controls (Fig. 2a; Supplementary Fig. 3a,b). qRT-PCR analysis showed lower *PAX6* expression and concomitantly higher *MAP2* and *SOX10* expression in SLOS iPSCs compared to controls, suggesting neuronal and neural crest specification, respectively (Fig. 2b). However, expression of *ALDH1L1*, a glia specific marker, was similar in all cultures (Fig. 2b). Extended differentiation assays revealed lower PAX6 expression in SLOS iPSCs relative to controls, along with continued expansion of βIII-tubulin networks (Supplementary Fig. 3c–e), formation of long neuronal projections (Supplementary Fig. 3f), and higher expression of neuronal transcripts *TUBB3*, *MAP2*, and *SYP* (Supplementary Fig. 3g–i).

Due to the neural progenitor defects and augmented neuronal differentiation observed in SLOS iPSCs, we wanted to determine if SLOS iPSC pluripotency was affected in cultures grown in cholesterol deficient medium. Control and SLOS iPSCs were shifted to feeder-independent cultures in cholesterol deficient mTeSR1 media for expansion in pluripotent conditions[13]. Control iPSCs maintained pluripotent morphology in mTeSR1; however, SLOS iPSCs exhibited a spindled, neural progenitor-like phenotype (Fig. 2c). Structural analysis of SLOS iPSCs cultured in mTeSR1 revealed fewer cell-to-cell contacts compared to hESCs and the generation of secondary filaments, indicators characteristic of loss of pluripotency compared with hESCs (Fig. 2d). To determine if cholesterol supplementation

would prevent loss of SLOS iPSC pluripotency, mTeSR1 cultured SLOS iPSCs were supplemented with 10 mcg cholesterol/mL medium with either high-density lipoprotein (HDL) or low-density lipoprotein (LDL). Immunocytochemical analysis revealed higher expression of the pluripotency marker TRA-1-81$^+$ in LDL-supplemented SLOS iPSCs compared to untreated or HDL-supplemented cultures (Fig. 2e,f). Confirming that this effect was not specific to mTeSR1, SLOS iPSCs cultured in XF-KSR medium, another feeder-independent, cholesterol deficient medium (1.85 ± 0.18 mcg cholesterol/mL), also exhibited precocious differentiation, as evidenced by low expression of TRA-1-81$^+$ (Fig. 2f). LDL supplementation also maintained SLOS iPSC gap and tight junctions and prevented secondary filament formation (Fig. 2d). Cholesterol supplementation also allowed for the formation of morphologically normal SLOS rosette structures comparable to control iPSCs (Fig. 2g). SLOS rosettes could be isolated and expanded as neural progenitor lines when cultured with continuous cholesterol supplementation. Expandable SLOS progenitors maintained robust SOX2 and hNestin expression without formation of βIII-tubulin$^+$ neurons (Fig. 2h).

To identify differentiation networks resulting from impaired endogenous cholesterol synthesis, SLOS iPSCs were analyzed for protein and transcriptional changes seven days after initiating cholesterol deficient culture. SLOS iPSCs exhibited loss of the pluripotent marker NANOG and emergence of PAX6$^+$ and hNestin$^+$ neural progenitors within differentiating cultures (Fig. 3a,c,d). Quantitative PCR confirmed lower expression of *POU5F1* (pluripotent marker) and higher expression of *PAX6* (CNS progenitor marker) and *SNAI2* (marker of neural crest and epithelial-mesenchymal transition) in SLOS iPSC lines (Fig. 3b). However, little change was observed in *VIM* (mesodermal/mesenchymal marker) or *AFP* (endodermal marker). Of note, the degree of aberrant differentiation and neural fate choice appeared to correlate with phenotypic severity. SLOS iPSCs from both moderately affected (CW and CWI) and severely affected (A2) subjects exhibited loss of pluripotency markers such as *POU5F1* and higher expression of the neural crest marker, *SNAI2*. However, relative to A2-derived lines, the iPSCs derived from moderate subjects demonstrated lower levels of expression of CNS progenitor markers (Fig. 3b,d).

Aberrant SLOS differentiation is caused by 7-dehydrocholesterol accumulation

To determine if aberrant neuronal differentiation in SLOS was due to low cholesterol or elevated 7DHC, hESCs were treated with inhibitors of cholesterol synthetic enzymes other than DHCR7, causing cholesterol loss without DHC accumulation. Treatment of hESCs with simvastatin, an HMG-CoA reductase inhibitor, induced SREBP2 dependent gene expression, confirming functional inhibition of endogenous cholesterol synthesis (Supplementary Fig. 3a). While treatment with simvastatin inhibited cellular proliferation, hESC morphology was maintained and no significant change in pluripotent or lineage specific transcript expression was observed (Supplementary Fig. 3b,c). Treatment of hESCs with U18666A to both inhibit desmosterol reductase (DHCR24) and induce endolysosomal accumulation of unesterified cholesterol[16] reduced cholesterol content and higher desmosterol levels. However, no change in hESC morphology or pluripotent and tissue specific gene expression was observed (Supplementary Fig. 4a,b,d). In contrast, treatment of hESCs with the DHCR7 inhibitor AY9944[17] caused marked accumulation of 7DHC and

induced aberrant neural differentiation similar to that observed in SLOS iPSCs (Supplementary Fig. 4a–c). AY9944 treatment also inhibited rosette formation and induced βIII-tubulin expression in control iPSC neural differentiation assays (Supplementary Fig. 5a,b).

To further address the specificity of defects in cholesterol homeostasis on aberrant differentiation observed in SLOS iPSCs, we generated iPSCs from subjects with either Niemann-Pick disease, type C1 (NPC1) or Lathosterolosis. In NPC1, intracellular cholesterol transport is impaired, resulting in endolysosomal accumulation of unesterified cholesterol and decreased intracellular cholesterol bioavailability[18]. Of note, elevated DHC levels in SLOS cells can induce an NPC-like accumulation of unesterified cholesterol[19]. While NPC1 iPSCs demonstrated increased filipin staining of unesterified cholesterol, they maintained a pluripotent morphology when cultured in either cholesterol replete or cholesterol deficient conditions (Supplementary Fig. 6a). Further, qRT-PCR analysis confirmed that no significant changes occurred in the expression of neural crest/epithelial-mesenchymal transition (*SNAI2*), neuroectoderm (*PAX6*), or pluripotency (*NANOG, POU5F1)* markers (Supplementary Fig. 6b). Lathosterolosis, an inborn error of cholesterol synthesis due to mutation of the lathosterol 5-desaturase (*SC5D*) gene, impairs conversion of lathosterol to 7DHC[20]. While both DHCR7 and SC5D deficiency result in decreased cholesterol levels, SC5D deficiency results in the accumulation of lathosterol rather than 7DHC. Lathosterolosis iPSCs exhibited lathosterol accumulation pluripotent transcript and protein expression comparable to hESCs, and maintained pluripotent morphology when cultured in either cholesterol replete or deficient conditions (Supplementary Fig. 7a–f).

7-dehydrocholesterol directly inhibits Wnt/β-catenin activity

To identify signaling pathways mediating aberrant neural formation in SLOS iPSCs, we performed a time-course, whole genome analysis of cDNA transcripts in control iPSCs versus SLOS iPSCs (Fig. 3e). Transcript expression was compared between cell lines and within cell lines over time to determine how control iPSCs and SLOS iPSCs respond to cholesterol deficient conditions. Comparative analyses revealed SLOS iPSCs cultured in cholesterol deficient conditions initiated transcriptional networks leading to epithelial-mesenchymal transition, initiation of neural differentiation, and loss of cadherin-associated signaling, kinase signaling, pluripotency, and Wnt signaling (Supplementary Table 2,3). Examining the earliest time points at the initiation of differentiation, we observed 44 genes differentially expressed between control and SLOS iPSCs. Within this differentially expressed gene cluster, a number are associated with Wnt/β-catenin signaling (including *CAV1*, *CDH1*, and *SNAI2*) (Fig. 3f,g), suggesting a likely role for Wnt/β-catenin signaling in SLOS iPSC neural specification.

Wnt signaling inhibits formation of the Axin/APC/GSK3β scaffolding complex and allows β-catenin accumulation[21,22], regulating neurogenesis[23], cortical differentiation[24], and hESC neural differentiation[25]. The PDZ domain of Dishevelled (DVL) binds cholesterol, an essential interaction for the scaffolding function of DVL[26]. To determine whether 7DHC might disrupt the cholesterol-dependent scaffolding function of DVL, we measured the binding of the DVL2-PDZ domain to plasma membrane (PM)-mimetic vesicles containing

cholesterol or 7DHC, respectively, by surface plasmon resonance analysis (Fig. 4a,b). The DVL2-PDZ domain exhibited 20-fold lower affinity for 7DHC-containing vesicles than for cholesterol-containing vesicles (Fig. 4b). To test whether 7DHC accumulation reduces the PM binding and scaffolding activity of DVL2 under physiological conditions, we monitored the dynamic colocalization of DVL2 and FZ7 in HeLa cells by simultaneous single molecule tracking that allows sensitive and quantitative detection of dynamic and transient interactions among signaling proteins[26,27]. Activation of FZ7 receptor by WNT3A dramatically enhanced the dynamic colocalization of Halo-TMR-labeled-FZ7 and EGFP-tagged DVL2 on the PM (Fig. 4c,d). Substitution of cholesterol in the PM with 7DHC by treatment of cells with the methyl-β-cyclodextrin (MβCD) - 7DHC complex greatly decreased the WNT3A-induced dynamic colocalization of DVL2 and FZ7 (Fig. 4c,d). In contrast, treatment of cells with the same ratio of the MβCD-cholesterol complex had little effect on the interaction of DVL2 and FZ7 (Fig. 4c,d). Similarly, WNT3A enhanced the dynamic colocalization of FZ7 and LRP6, which was abrogated by treatment with MβCD-7DHC but not MβCD-cholesterol (Fig. 4e). These results support the notion that 7DHC accumulation inhibits canonical Wnt/β-catenin signaling by interfering with PM binding and the scaffolding function of DVL.

Stabilization of β-catenin activity prevents aberrant SLOS iPSC differentiation

We next investigated whether altered Wnt/β-catenin signaling could underlie the aberrant SLOS iPSC neural differentiation. Treatment of SLOS iPSCs in cholesterol deficient conditions with the GSK3β inhibitor CHIR99021 prevented loss of pluripotent morphology, while controls exhibited mild differentiation, suggesting that optimal cellular levels of β-catenin are essential for pluripotent maintenance (Fig. 5a). Either recombinant Wnt3A or CHIR99021 treatment stabilized expression of active β-catenin comparable to cholesterol replete conditions and maintained total β-catenin expression similar to hESCs (Fig. 5b). To determine if β-catenin maintenance prevented SLOS iPSC differentiation, we quantitated colonies for TRA-1-60 expression. CHIR99021 treatment, without cholesterol supplementation, prevented loss of pluripotency comparable to LDL treatment (Fig. 5c).

To examine the consequences of β-catenin stabilization in SLOS iPSCs, we analyzed CHIR99021 effects on proteins associated with Wnt signaling, cell-cell contact, and pluripotency. CHIR99021 induced expression of the phosphorylated active form of the Wnt signaling co-receptor LRP6, active β-catenin, OCT4, and E-cadherin (Fig. 5d,e and Supplementary Fig. 8). CHIR99021 effects were more robust than LDL supplementation, suggesting loss of Wnt/β-catenin activity likely initiates SLOS iPSC neural differentiation. Further, the molecular response of iPSCs derived from severe (A2) versus moderate (CWI) phenotype subjects suggests the degree of DHCR7 inhibition may discriminately affect Wnt/β-catenin signaling events, supporting the phenotype dependent differentiation observed. DHCR7 effects on Wnt signaling were not restricted to iPSCs, as additional analyses demonstrated reduced β-catenin activity in SLOS iPSC rosette assays (Fig. 5g), AY9944 treated control iPSC rosette assays, and the cerebral cortex of *Dhcr7*$^{-/-}$ mice (Fig. 5f and Supplementary Fig. 8e,f). However, we did not observe altered β-catenin activity in Lathosterolosis iPSCs, which maintained pluripotency and β-catenin activity in both cholesterol replete and cholesterol deficient conditions (Fig. 5h).

To determine if the aberrant differentiation of SLOS iPSCs has an *in vivo* correlate, we examined proliferation and cortical layer formation within *Dhcr7*$^{-/-}$ mice. Quantitation of Nissl staining and Ki67^{+} proliferating cells revealed layering defects within the subventricular and intermediate zones of the E18.5 cortex (Supplementary Fig. 9a–c) and a loss of Ki67 expression within outer cortical layers (Supplementary Fig. 9d–f).

Isogenic control for effects of DHCR7 on β-catenin activity

To confirm DHCR7 effects on Wnt/β-catenin signaling in a pluripotent isogenic cell line, we targeted the exon 8/intron 9 boundary of the DHCR7 locus with CRISPR/Cas9 nucleases in hESCs (Fig. 6a). Following nucleofection and antibiotic selection of transfected clones, a hESC clone (designated H1:*DHCR7*^{Mut}) was found to contain a single nucleotide insertion at the 5′ position of exon 9 (c.1237_38insG), altering the reading frame of *DHCR7* and eliminating the stop codon at c.1699_1701 (Fig. 6a). We observed no insertion/deletion events at ten predicted off-target sites assayed by Sanger sequencing (Supplementary Fig. 10). This clone maintained a normal karyotype and expression of pluripotency markers over multiple passages in cholesterol-replete conditions. To determine if this insertion event would induce SLOS-like biochemical defects, we cultured H1:*DHCR7*^{Mut} iPSCs in cholesterol deficient mTeSR1 and analyzed by GC/MS. H1:*DHCR7*^{Mut} recapitulated the SLOS biochemical defect (Fig. 6b). qRT-PCR analysis of H1:*DHCR7*^{Mut} maintained in cholesterol deficient conditions confirmed patterns of differentiation similar to SLOS iPSCs, including significant upregulation of *PAX6* and *SNAI2*, markers of neuroectoderm and neural crest differentiation (Fig. 6c). Lastly, while H1:*DHCR7*^{Mut} iPSCs maintained pluripotent morphology and high β-catenin activity in cholesterol replete medium, cholesterol deficient culture in mTeSR1 induced differentiation to a neural progenitor-like phenotype, upregulation of hNestin, and attenuation of β-catenin activity (Fig. 6d).

Discussion

We have utilized iPSC neural derivatives to identify a previously unrecognized cellular defect associated with SLOS. Our data strongly support a model where 7DHC disruption of DVL scaffolding function leads to dysregulated Wnt/β-catenin activity (Fig. 6e). Dysregulated Wnt/β-catenin activity in turn results in precocious neural differentiation of SLOS iPSCs and suggests progenitor defects may contribute to the SLOS neural phenotype. Within the CNS, altered Wnt/β-catenin has distinct effects on fate choice in radial glia and intermediate cortical progenitors, suggesting these effects may be cell type or niche dependent[24,29]. β-catenin regulates neural progenitors within the cerebral cortex and affects excitatory neuronal formation[29–31]. Loss of neural progenitor maintenance is consistent with the microcephalic phenotype observed in SLOS patients[1]. Wnt signaling defects may contribute to the functional and developmental defects found in *Dhcr7*$^{-/-}$ mouse excitatory neurons[14] and neurodevelopmental malformations/dysfunction observed in SLOS subjects[1]. Future work in inborn errors of cholesterol synthesis will need to discern the specific effects of cholesterol synthesis mechanisms on β-catenin dependent (canonical) versus β-catenin independent (non-canonical) Wnt signaling in neural phenotypes[32]. Further, recently identified defects in Wnt/β-catenin signaling associated with autistic symptoms[33,34] suggests the potential for broader implications of sterol/Wnt signaling interactions. It is also unclear

how cholesterol and Wnt interactions may affect disease pathogenesis through progenitor defects or differentiation in non-neural tissues[35,36]. Utilization of SLOS iPSCs will enable further exploration of these effects.

Our work using multiple iPSC models of cholesterol synthesis disorders and small molecules reveals significant differences in cell fate choices between these diseases in response to cholesterol deficient conditions, highlighting the complex and varied phenotypes underlying cholesterol synthesis disorders. Our findings also highlight the utility of iPSCs for modeling rare diseases and the identification of previously unrecognized signaling mechanisms underlying disease pathology. These studies provide a necessary framework for comparison of neurodevelopmental pathology in disorders of cholesterol synthesis with other neurological syndromes.

Online Methods

Reagents and cell culture

Human ES and iPSCs were maintained on inactivated mouse embryonic fibroblasts (MEF; Global Stem) in hESC media: DMEM/F12 base, 2 mM L-glutamine, 20% Knockout Serum Replacement, 1% NEAA, 1,000 units/mL Penicillin-streptomycin, 100 μM β-mercaptoethanol (Life Technologies), and bFGF (7.5 ng/ml; Stemgent). Feeder-free cultures were maintained in mTeSR1 (Stem Cell Technologies) on hESC-qualified Matrigel (BD Biosciences) coated culture dishes or chamber slides. Colonies were routinely passaged with dispase (1 mg/mL; Stem Cell Technologies) or manual dissection. Cultures were routinely analyzed by PCR for mycoplasma contamination/DNA (Universal Mycoplasma Detection Kit; ATCC). To begin cholesterol deficient pluripotent culture, colonies were either passaged by manual dissection or dispase treatment, rinsed with DMEM/F12, and transferred in mTeSR1 to Matrigel coated dishes. Dispase passage of cells growing in mTeSR1 utilized ROCK inhibitor supplementation (Y27632; 10 μM; Reagents Direct) for 24 h. Though the complete formulation of mTeSR1 designates it as maintaining low cholesterol content (1.12E-03 mM; 0.433 μg cholesterol/mL), mTeSR1 was batch tested for maintenance of hESC pluripotent morphology and analyzed by GC/MS for μg cholesterol/mL media. Small molecules and recombinant proteins used in this study include: Wnt3A (100 ng/mL; R&D systems), CHIR99021 (3 μM; Reagents Direct), AY9944 (2.5 μM) and U18666A (100 nM; Sigma-Aldrich). High-density lipoprotein (HDL; density 1.063 – 1.21 g/mL) and low-density lipoprotein (LDL; density 1.019 – 1.063 g/mL) were isolated from human plasma by sequential ultracentrifugation and dialysis, as previously published[37]. Research strictly adhered to federal regulations and NIH policies regarding the responsible use of human pluripotent stem cells. Human ESC lines WA01 and WA09 have been approved for federal use and can be found on the NIH Human Embryonic Stem Cell Registry (#0043 and #0062). The collection of clinical samples was approved by the Institutional Review Board of the *Eunice Kennedy Shriver* National Institute of Child Health and Human Development. Permission from guardians and assent, when possible, were obtained from all participants. Clinical studies under which fibroblasts were collected are posted on ClinicalTrials.gov (NCT00001721, NCT00046202 and NCT00344331).

Lentiviral reprogramming of subject fibroblasts

Skin punch biopsies were collected from SLOS and Lathosterolosis subjects according to NIH policies under IRB protocol number 98-CH-0081, 02-CH-0311 and 06-CH-0186. BJ human neonatal fibroblasts (Cat. No. CRL-2522; ATCC) and human lung fibroblasts (Cat. No. GM05387; Coriell Institute) were used to generate control iPS lines designated BJ and HDF, respectively. Control iPS lines SCU i19 and SCU i21 were a kind gift from Barbara Mallon and the NIH Stem Cell Unit. Fibroblasts were expanded and reprogrammed to pluripotency via lentiviral transduction with 3-factor (OCT4, SOX2, KLF4) or 4-factor (OCT4, SOX2, KLF4, c-MYC) STEMCCA reprogramming plasmid (kind gift from Dr. Gustavo Mostoslavksy, Boston University) using published methods[11]. Following viral transduction, fibroblasts were passaged to MEF coated 100 mm dishes and cultured for an additional 21 – 42 d. Individual clones were manually isolated and transferred to MEF coated 6 well dishes for expansion. Transgene excision was performed by FuGene HD (Roche) transfection of iPSCs with Cre-IRES-PuroR (gift from Darrell Kotton; Addgene; plasmid 30205)[11], followed by puromycin (Sigma) selection.

Immunocytochemistry

Cells plated to chamber slides were fixed in 4% PFA for 15 min at room temperature, washed with PBS, and permeabilized with 0.2% Triton X-100 (Sigma) in PBS (PBS-T) for 20 min. To limit non-specific binding, cells were incubated for 1 h in 5% normal donkey or goat serum (Cell Signaling) diluted in PBS-T (blocking buffer). Cells were incubated overnight in blocking buffer containing the following primary antibodies: rabbit anti-Nanog (1:400; Cell Signaling; D73G4), rabbit anti-Oct4A (1:400; Cell Signaling; C30A3), mouse anti-SSEA4 (1:400; Cell Signaling; MC813), mouse anti-Tra-1-60 (1:400; Cell Signaling; TRA-1-60), mouse anti-Tra-1-81 (1:400; Cell Signaling; TRA-1-81), rabbit anti-Sox2 (1:400; Cell Signaling; D6D9), rabbit anti-E-cadherin (1:1,000; Cell Signaling; 24E10), mouse anti-Pax6 (1:2,000; Developmental Studies Hybridoma Bank; PAX6), mouse anti-βIII-Tubulin (1:2,000; Millipore; MAB1637), mouse anti-active β-catenin (1:1,000; Millipore; 05-665), mouse anti-human Nestin (1:2,000; Millipore; MAB5326), goat anti-Nkx2.5 (1:200; Santa Cruz Biotechnologies; SC-14033), and goat anti-GATA4 (1:200; Santa Cruz Biotechnologies; SC-1237). Cells were rinsed and primary antibodies detected with 555 donkey anti-rabbit IgG (1:500; Life Technologies; A-31572), 555 donkey anti-mouse IgG (1:500; Life Technologies; A-31570), 488 goat anti-rabbit IgG (A-11008), 488 goat anti-mouse IgG (1:500; Life Technologies; A-11001), or 555 donkey anti-goat (1:500; Life Technologies; A-21432). Nuclei were counterstained with Hoechst 33342 (Life Technologies). Slides were mounted with ProLong Gold Antifade (Life Technologies) prior to imaging with a Leica DMI4000B or Leica DM6000B microscope. Images were processed with Volocity (PerkinElmer) and Adobe Photoshop (Adobe Systems) software. TRA-1-60 and TRA-1-81 positivity was quantitated based on > 50% of colony area exhibiting both pluripotent morphology and positive staining.

Real-time qRT-PCR

Samples were collected via centrifugation and RNA isolated using PicoPure Isolation kit (Life Technologies) with DNase I (Qiagen) per manufacturer instructions. cDNA was

generated from 1 μg RNA via SuperScript III First-Strand Synthesis kit (Life Technologies). Real-time qPCR was performed using custom designed primers and SYBR Green I Master mix (Roche) on a Lightcycler 480. Expression levels were normalized to *GAPDH* expression. Primer sequences used to detect endogenous expression of *KLF4* and *SOX2* were previously published[38]. Custom designed primer sequences used are available upon request.

Teratoma formation and analysis

Teratoma assays were performed by Applied Stem Cell (Menlo Park, CA). Control and patient iPSCs in hESC media on a MEF feeder layer were harvested by 1 mg/mL dispase, collected by centrifugation, and resuspended in 30% Matrigel. iPSCs (1.5×10^6) were injected under the kidney capsule and testis of three nonobese diabetic (NOD)/severe-combined immunodeficient (SCID) mice for BJ 3F-1 control iPS and A2 3F-2 SLOS iPS cell lines. Tumors developed within 4–8 wk, at which time they were isolated after sacrificing the mice and formalin fixation. After sectioning, teratomas were analyzed for germ layer formation on the basis of hematoxylin and eosin staining.

Analysis of patient-specific mutations in *DHCR7* and *SC5D*

DNA was isolated using the DNeasy kit (Qiagen), confirmed for quality by Nanodrop analysis, and analyzed for patient-specific mutations using previously published primer sequences and PCR conditions[2,20,39]. For Sanger sequencing, 100 ng DNA was used for each PCR reaction utilizing primers spanning *DHCR7* regions with known mutations. 1 – 5 μL of PCR reaction was purified with Exosap-IT (Fisher Scientific). 4 μL of Exosap reaction product was mixed with BigDye Terminator Mix (Applied Biosystems), buffer and primers, followed by the following reaction conditions: 96 °C for 10 s, 50 °C for 10 s, 60 °C for 4 min. This cycle was repeated 30 times followed by Sephadex G50 (Sigma-Aldrich) purification of PCR fragments. Sequencing was performed on a 3130x1 Sequencer (Applied Biosystems) and chromatograms exported using SnapGene.

Gas chromatography/mass spectrometry in hESCs and iPSCs

Cell pellets flash frozen on dry ice received 1 mL water and were lysed by freeze/thaw method in a 55 °C water bath. 100 μL per sample was removed and analyzed for protein concentration by Bradford assay (BioRad). 1 mL buffer containing 92% C_2H_6O, 7% KOH, and 1% coprostan-3-ol (Sigma) was added per sample, shaken, and saponified at 60 °C for 1 h. 1 mL water was then added per sample, followed by organic extraction with 3 mL ethyl acetate. Samples were vortexed, centrifuged, and the organic phase removed. Samples were then dried by heating at 60°C concurrent with nitrogen gas flow for lipid isolation. Extracted lipids were derivatized with 50 μL Pyridine CHROMASOLV Plus (Sigma) and 50 μL N,O-bis(trimethylsilyl) trifluoroacetamide (BSTFA) with 1% trimethylchlorosilane (TMCS) (Pierce Biotechnology) per sample, followed by 1 h incubation at 60 °C. Samples were then transferred to amber tubes and sterol levels measured on an Ultra Trace GC (Thermo Scientific). Analysis was performed with XCalibur software (Thermo Scientific). Peak identification for specific sterols was based on known sterol retention time, retention time of coprostanol as an internal standard (~14 min), and comparison to the National Institute of Standards and Technologies Standard Reference data set. For peak quantitation, the area

under the curve for individual sterols was divided by the area under the curve for coprostanol. Results from analyses of cholesterol levels were normalized to protein concentration measured by Bradford assay and represented as μg sterol/ mg protein. After quantification of individual sterol content, data is presented as the fraction of dehydrocholesterol (7DHC + 8DHC) to total quantified sterols. This allows for comparison of biochemical severity across cell lines and experiments independent of variable growth conditions which may influence total sterol synthesis.

Germ layer and neural differentiation of iPSCs

For *in vitro* germ layer differentiation, embryoid bodies (EBs) were generated by dissociating colonies to single cells using dispase, cells were counted, and 1×10^6 cells were plated per well of AggreWell 800 dish (Stem Cell Technologies) in bFGF-deplete ES media with 10 μM Y27632. After 24 h culture, generated EBs were gently collected and transferred to 6 well low binding dishes (Nunc) containing differentiation media (hESC media minus bFGF). Cells were fed 24 h later, cultured an additional 4 days, and then spotted individually to gelatinized dishes. Twelve days after plating, cultures were fixed for immunocytochemistry or collected via scraping for RNA isolation, cDNA synthesis, and qRT-PCR.

For neural differentiation assays, EBs were generated in hESC media plus 20 ng/ml bFGF using AggreWell 800 dishes as above. After 24 h culture, generated EBs were gently collected and transferred to low binding dishes containing hESC media plus 20 ng/mL bFGF. Cells were fed 24 h later and after culture for 3 additional days in low binding dishes, media was changed to neural induction media (NIM): DMEM/F12 base, 2 mM L-glutamine, N2A, 1% NEAA, and 1,000 units/mL Penicillin-streptomycin (Life Technologies) for an additional 2 d. Neuralized EBs were plated to laminin (20 μg/mL;) coated dishes for rosette formation and terminal differentiation. For rosette formation and early neuronal quantitation, neuralized EBs were immunostained for mouse anti-Pax6 (1:2,000; DSHB), rabbit-anti Sox2 (1:400; Cell Signaling; D6D9), and mouse anti-βIII-tubulin (1:2,000; Millipore; MAB1637) 3–4 days after initiating terminal differentiation. Primary antibodies were detected with donkey anti-rabbit 555-IgG (1:500; Life Technologies; A31572) or goat anti-mouse 488-IgG (1:500; Life Technologies; A11001). ‘Early neuronal differentiation’ was quantitated in individual EBs based on the presence or absence of βIII-tubulin expression.

Karyotypic analysis of ES and iPS cell lines

All assays of chromosomal integrity were performed by the NHGRI Cytogenetics Core facility. DNA spectral karyotyping (SKY) was performed according to manufacturer protocols (Applied Spectral Imaging, Carlsbad, CA). G and C-banding was obtained and analyzed as previously published[40]. All cell lines were analyzed at early passage (< P10) and continuously monitored for karyotypic integrity.

Electron microscopy

Human ESCs and iPSCs were dissociated with dispase and plated to Aclar embedding film (Ted Pella, Inc.) coated with Matrigel. Cells were cultured for 3 d in mTeSR1 media and fixed with 2.5% glutaraldehyde in 0.1 M sodium cacodylate buffer. Samples were processed

and imaged with the assistance of the NICHD Microscopy and Imaging Core. Following fixation and buffer rinse, cells were further processed in a variable wattage Pelco BioWave Pro microwave oven (Ted Pella, Inc.). Cells were post-fixed in 1% osmium tetroxide in 0.1 M sodium cacodylate buffer, dehydrated in increasing concentrations of ethanol, and infiltrated into increasing concentrations of Spurr's resin (Electron Microscopy Sciences) via ethanol. Cells were then embedded and polymerized in 100% resin for 18 h in a lab oven set at 70 °C. 90 nm thick sections were prepared on a Reichert-Jung Ultracut-E ultramicrotome using a Diatome diamond knife. Grids were post-stained with uranyl acetate and lead citrate and examined in a JEOL 1400 transmission electron microscope operating at 80 kV.

Flow cytometry of iPSCs

Cells cultured in mTeSR1 for 4 or 7d were immunostained for mouse anti-β-catenin/555 conjugated (1:50; Cell Signaling; L54E2) or mouse anti-hNestin/FITC conjugated (1:50; R&D Systems; IC1259F), respectively. Cells were collected with accutase, rinsed, and fixed in 2% PFA overnight at 4°C. Cells were rinsed with 0.1% BSA/PBS, treated with 0.1% Triton X-100/0.1% BSA/PBS for 15 min, rinsed, and incubated for 2 h in primary antibody diluted in 2% goat serum while shaking. 488-IgG (1:100; Cell Signaling; 2975S) and PE-IgG (1:100; Cell Signaling; 5742S) were used as isotype controls. Cells were rinsed, resuspended in 0.1% BSA/PBS, and analyzed on a FACS Caliber (BD Biosciences). Analysis was performed using CellQuest Pro (BD Biosciences) and FlowJo (Tree Star, Inc.) software.

Whole-genome microarray analyses of control and patient iPS cell lines

RNA was isolated using the PicoPure isolation kit. RNA quality and quantity was ensured using a Bioanalyzer (Agilent, Inc.) and NanoDrop (Thermo Scientific). For RNA labeling, 2 μg of total RNA was enriched with RiboMinus kit (Life Technologies) and the Affymetrix recommended Whole-Transcript Expression Analysis protocol. The hybridization cocktail containing fragmented and labeled cDNAs was hybridized to Human Exon 1.0 ST chips (Affymetrix). Chips were washed and stained by the Affymetrix Fluidics Station using standard format and manufacturer protocols. Probe arrays were stained with streptavidin phycoerythrin solution (Molecular Probes) and enhanced by an antibody solution containing 0.5 mg/mL of biotinylated anti-streptavidin (Vector Laboratories). Gene Chip Scanner 3000 (Affymetrix) was used to scan the probe arrays. Gene expression intensities were calculated using Affymetrix AGCC software. Partek was used to normalize via robust multi-array average and analyze the microarray data for differentially expressed genes. Fold change was calculated between all pairs of replicates. Given that the distributions of the fold changes for all replicate pairs was normally distributed and centered around 0, we calculated the mean + 2*standard deviation to find the upper threshold of the fold change distributions. Benjamini-Hochberg adjusted p-values < 0.05 were used to show statistical significance.

Filipin staining of NPC iPS cells

NPC iPSCs were dissociated with dispase and plated to MEF or Matrigel coated chamber slides containing hESC media or mTeSR1, respectively. Cells were cultured for 4 d then processed for immunocytochemistry. Chambers were fixed with 4% PFA for 30 min, PBS rinsed, permeabilized with 0.2% saponin (Sigma) in 10% goat serum, PBS rinsed, and

incubated overnight at 4 °C with 50 μg/mL freshly prepared filipin (Sigma) and rabbit anti-OCT4A diluted in 0.05% saponin/10% goat serum. Cells were rinsed and primary antibody detected with goat anti-rabbit 555 IgG diluted in 0.05% saponin/10% goat serum/50 μg/mL filipin. Slides were mounted, imaged with a Leica DM6000B microscope, and processed with Volocity (PerkinElmer) and Adobe Photoshop (Adobe Systems) software.

SDS-page/Western blot analysis of human ESCs, iPSCs, and *Dhcr7* brain tissue

Protein was isolated with cOmplete Lysis-M plus protease/phosphatase inhibitors (Roche) and quantitated by Bradford assay (BioRad). 50 μg protein was separated in 4–12% Bis-Tris mini-gels (Life Technologies), transferred to nitrocellulose membranes via iBlot (Life Technologies), and blocked in 5% BSA diluted in 1x TBS-0.1% Tween (TBS-T) for 1 h while rocking. The following primary antibodies diluted in 5% BSA were incubated overnight at 4 °C: rabbit anti- LRP6 (1:2,000; Cell Signaling; C47E12), rabbit anti-phospho-LRP6 (1:2,000; Cell Signaling; S1490), rabbit anti-OCT4A (1:2,000; Cell Signaling; C30A3), rabbit anti-β-catenin (1:2,000; Cell Signaling; D10A8), mouse anti-active β-catenin (1:2,000; Millipore; 05-665), and mouse anti-β-actin (1:20,000; Sigma; A3853). Membranes were rinsed in TBS-T, followed by incubation with HRP-goat anti-mouse IgG (1:20,000; Sigma-Aldrich; SAB3700993) and HRP-donkey anti-rabbit IgG (1:20,000; Sigma-Aldrich; SAB3700978) for 1 h while rocking. Membranes were rinsed in TBS-T, detected with Clarity Western ECL (BioRad), and exposed in a ChemiDoc XRS+ system (BioRad).

CRISPR/Cas9 cloning and DHCR7 targeting

The pX330-U6-Chimeric_BB-CBh-hSpCas9 plasmid was a gift from Feng Zhang (Addgene; plasmid #42230)[41]. Generation of *DHCR7* targeted Cas9 followed the general protocol for use of the pX330 plasmid using the online resource developed by Dr. Feng Zhang's laboratory at the Massachusetts Institute of Technology (http://www.genome-engineering.org/)[41]. Briefly, the pX330 plasmid was digested in a 40 μL reaction with 2 μL Bbs1 for 60 min at 37 °C. Digested pX330 was gel purified using the QIAquick Gel Extraction kit (Qiagen) and resuspended in EB buffer. The following gRNAs were designed using online CRISPR design software (http://crispr.mit.edu/), annealed, and ligated to the linearized pX330: Forward gRNA, 5′ - TACACCAAGTACAGACCCTG - 3′; Reverse gRNA, 5′ - CAGGGTCTGTACTTGGTGTA - 3′. Off-target prediction software identified no coding regions other than DHCR7 with < 3 base pair mismatches to the guide sequence, which has been suggested to limit off-target effects of the CRISPR system[42]. gRNAs were incubated with T4 ligation buffer for annealing, ligated with Quick Ligase, and transformed in competent E. coli. Ampicillin resistant clones were selected, amplified, and purified by miniprep (GeneJet). Clones were sequenced based on the U6 promoter targeted primer: 5′ - GAGGGCCTATTTCCCATGATTCCTTC – 3′.

CRISPR/Cas9 editing of H1 ES cells

H1 ES cells growing on MEF feeders were pre-incubated with 10 μM Y27632 for 30 min, feeders were manually removed, and H1 ES cells isolated with Accutase (Life Technologies). $1x10^6$ H1 cells were resuspended in Nucleofection buffer V containing 5 μg *DHCR7* targeted pX330 and 1 μg puromycin resistant plasmid in electrode cuvettes. Cells were transfected using the Nucleofector 2b system (Lonza), program A-23. Cells were

plated to DR4 MEF coated dishes and puromycin selection (1.25 μg/mL) was begun 24 hours post-transfection. Puromycin selection was stopped after 48 hours and individual clones manually selected approximately 7 d later. Individual clones were expanded and screened for insertion/deletion events by Sanger sequencing and GC/MS analysis.

Off-target genomic analysis of CRISPR/Cas9 edited H1 clones

Predicted off-target genomic sequences were determined using online software (crispr.mit.edu) as previously published[43]. Of the top 30 potential off-target sites based on the likelihood of probe binding, five fell within exonic regions for coding genes. Each of these five exonic targets, as well as the top five predicted non-coding sequences, were amplified by PCR and analyzed by Sanger sequencing. Genomic DNA was isolated using the DNeasy purification kit and PCR amplified using the following oligonucleotide pairs: off-target #1 Forward 5′ – CTCAACAGTTTCCTTGTACCCACC – 3′, Reverse 5′ – TCAGAGACCAGTGAAAAAGCTGTG – 3′; off-target #2 Forward 5′ – CTGCTTTTTCATGCACCCTTCTTT – 3′, Reverse 5′ – GATGGCATGGATGGAGGCTT – 3′; off-target #3 Forward 5′ – ACAAGATATAACTGTGGCTTTTCAC – 3′, Reverse 5′ – TCATTGAAGTCTCCATTAATTCTGC – 3′; off-target #4 Forward 5′ – TAAGCCGCACAACCTAAGCA – 3′, Reverse 5′ – CTGCACATTCTCCTCCCCAG – 3′; off-target #5 Forward 5′ – AGAAAAGGAAGACGGCTCCA – 3′, Reverse 5′ – TCCTCACATCACCCTCAAAGG – 3′; off-target #6 Forward 5′ – AGTGAAAGTGAAGTACATTGCATC – 3′, Reverse 5′ – ACCTTCTTGGAACTGAAACACA – 3′; off-target #7 Forward 5′ – GCTGTCTTGCCCTAACCACAT – 3′, Reverse 5′ – GCTTTTAACCTGGGCATCCGA – 3′; off-target #8 Forward 5′ – CTGTGTGGTGCCTAGACCTG – 3′, Reverse 5′ – AGCTCTCAGCAAACTGGGTC – 3′; off-target #9 Forward 5′ – TTGGGCCAGGAATGCAAGTAT – 3′, Reverse 5′ – ACTAATTCTCAGCAAAGGAGAGGAA – 3′; off-target #10 Forward 5′ – TGCATGAGTTACTGACTCTTCTCT – 3′, Reverse 5′ – AGATGTTGGCTGTTTAACCTTCT – 3′. PCR products were purified using the PureLink PCR Purification kit (ThermoScientific), Sanger sequencing was performed (Eurofins MWG Operon), and results visualized using SnapGene software.

Protein and vesicle preparation for surface plasmon resonance analysis

The DVL2 PDZ domain was bacterially expressed in a purified form as described before[26]. PM-mimetic vesicles were prepared by mixing 1-palmitoyl-2-oleoyl-sn-glycero-3-phosphocholine (POPC), 1-palmitoyl-2-oleoyl-sn-glycero-3-phosphoethanolamine (POPE), 1-palmitoyl-2-oleoyl-sn-glycero-3-phosphoserine (POPS), cholesterol, 1-palmitoyl-2-oleoyl-sn-glycero-3-phosphoinositol (POPI), and 1,2-dipalmitoyl derivatives of phosphatidylinositol-(4,5)-bisphosphate (PtdIns(4,5)P_2) in a molar ratio of 12:35:22:22:8:1. Large unilamellar vesicles with 100 nm diameter were prepared with a microextruder (Avanti) using a 100 nm polycarbonate filter.

Surface plasmon resonance (SPR) analysis

All SPR measurements were performed at 23 °C in 20 mM Tris-HCl, pH 7.4, containing 0.16 M KCl using a lipid-coated L1 chip in the BIACORE X system as described

previously[44,45]. PM-mimetic vesicles containing cholesterol (or 7-dehydrocholesterol) and POPC vesicles were used as the active surface and the control surface, respectively. Vesicles were injected at 5 μl/min onto the corresponding sensor chip surfaces to yield the identical resonance units (RU), ensuring the equal concentration of the coated lipids. Equilibrium measurements were performed at a flow rate of 5 μL/min, which allowed enough time for the R values of the association phase to reach near equilibrium levels (R_{eq})[46]. Each sensorgram was background-corrected by subtracting the control surface response from the active surface response. A minimum of 5 different protein concentrations was injected to collect a set of R_{eq} values plotted against the protein concentrations (P_o). An apparent dissociation constant (K_d) was then determined by nonlinear least squares analysis of the binding isotherm using the equation, $R_{eq} = R_{max} / (1 + K_d/P_o)$ where R_{max} indicates the maximal R_{eq} value[47]. Since the concentration of lipids coated on the sensor chip cannot be accurately determined, K_d is defined as P_o yielding half-maximal binding with a fixed lipid concentration. Each measurement was repeated ≥ 3 times to determine average and standard deviation values. For kinetic measurements, the flow rate was maintained at 20–30 μL/min.

Single molecule imaging in HeLa cells

Simultaneous single molecule imaging of two proteins was performed in HeLa cells using a TIRF microscope custom-built on the Olympus IX71 microscope base[27]. One protein is tagged with EGFP (on either N- or C-terminus) and the other by Halo™ (Promega), which was labeled with Halo-Tag TMR (Promega)[27]. For efficient expression of EGFP-LRP6, a LRP6-chaperone protein MESD[48] was co-transfected into HeLa cells. Two DPSS laser sources (488 and 561 nm, Excelsior, Spectra-Physics) were used and the fluorescence signal from the sample was split into two channels, passed through emission filters (510BP20, Omega and D630/30, Chroma), and projected onto two Andor iXon 897 EM-CCD cameras. The images were spatially corrected following the algorithm described previously[49]. All particle tracking, data analysis, and image processing were carried out with in-house programs written in MATLAB. Co-localization analysis of two molecules was performed with a fixed threshold criterion (i.e., < 400 nm) for co-localization[49]. An identical plasma membrane surface area was analyzed for each data point. The percentage of DVL2 (or LRP6) molecules spending a given colocalization time (> 0.2 s) with FZ7 on the plasma membrane was calculated from the total number of DVL2 (or LRP6) molecules and displayed as a histogram. Data were fit into a single exponential decay equation (i.e., $P = P_o e^{-kt}$) to determine the dissociation rate constant (k) values by non-linear least-squares analysis and the half-life values of co-localization were calculated as $\ln 2/k$. P and P_o indicate partial and total protein population. 50–100 images were analyzed for each data point. Cholesterol extraction and reloading was performed by the methyl-β-cyclodextrin (MβCD)-cholesterol complex[50]. Briefly, 5 mM MβCD saturated with 7-dehydrocholesterol (or cholesterol) in lipoprotein-deficient serum-free Dulbecco's Modified Eagle's medium was vortexed and 0.45-μm filtered. Cells were rinsed three times with 2 mL of serum-free Dulbecco's Modified Eagle's medium and incubated with 150 μL of MβCD-7-dehydrocholesterol solution for 60 min in a humidified CO_2 incubator at 37 °C prior to single molecule imaging.

Mice

The C57/BL6 mouse strain (Jackson Laboratories) was used for all animal studies performed at the National Institutes of Health. All mice in this study were handled according to protocols approved by the Institutional Animal Care and Use Committee of *The Eunice Kennedy Shriver* National Institute of Child Health and Human Development (ASP 12-002). *Dhcr7*$^{-/-}$ mice were identified by genotyping as previously described[51]. Mice of either sex were used for analyses. No statistical method was used to predetermine sample size for animal experiments.

Histology and immunohistochemistry

Dissected brains from transcardially perfused E18.5 embryos were processed for frozen coronal sections as described previously[52]. Nissl staining (Neurotrace 530/615; Life Technologies) was performed as follows: sections were warmed, rehydrated with PBS, treated with 0.1% PBS-T for 10 min, Neurotrace stained at 1:50 for 20 min, 10 min 0.1% PBS-T, counterstained with Hoechst, and mounted with ProLong Gold antifade. The thickness of the ventricular zone (VZ), subventricular zone (SVZ), intermediate zone (IZ), and cortical plate (including subplate and marginal zone) of the frontal lobe of the cerebral cortex were quantified in *Dhcr7*$^{+/-}$ and *Dhcr7*$^{-/-}$ mice using ImageJ. Individual layer thickness was quantified at 4 locations between the lateral ventricle and marginal zone of the frontal cortex for each section and represented as a ratio of layer thickness/total thickness. These values were averaged to give mean thickness ratio for each layer in each section. Coronal sections were closely matched between controls and mutants based on the E18.5 Developing Mouse Brain Atlas (Allen Brain Atlas). Three mice from two litters for both *Dhcr7*$^{+/-}$ and *Dhcr7*$^{-/-}$ mice were analyzed, utilizing 3 matched sections and 4 measurements per mouse.

For Ki67 quantitation, E18.5 brain tissue was processed as above as frozen sagittal sections. Rabbit anti-Ki67 (1:1,000; Abcam; AB15580) was incubated overnight at 4 °C in 5% normal goat serum diluted in 0.2% Triton X-100/PBS. Slides were rinsed in PBS-T, Ki67 detected with goat anti-rabbit-IgG DyLight 594 (1:1,000; Vector; DI-1594-1.5), and mounted with ProLong Gold antifade. Nuclei were counterstained with Hoechst 33342. Images of neocortical areas VZ, SVZ, and cortex (including the marginal zone, subplate and intermediate zone) were processed using ImageJ. Regions of the neocortex were manually drawn with the polygon tool and volume quantified. Ki67 positive cells were counted using the default threshold, watershed separation and analyze particles tool, and normalized to mm^2 for each zone. Imaging was performed using a Zeiss AxioObserver microscope and processed with Zeiss Zen and ImageJ software. Three mice from two litters were analyzed for both *Dhcr7*$^{+/+}$ and *Dhcr7*$^{-/-}$ groups, with 3 cortical cross-sections measured per mouse.

Statistical analysis

Statistical analyses were performed with Prism software (GraphPad) using unpaired Student's *t* test unless otherwise noted. Due to small sample size, normal distribution and equal variance was assumed. *P* values less than 0.05 were considered significant. All error bars represent standard error from the mean unless otherwise noted. No statistical method was used to predetermine sample size. The experiments were not randomized and

researchers were not blinded to allocation during experiments or when assessing outcomes. No samples or animals were excluded from analyses. Unless otherwise stated, ≥ 3 independent experiments were used for all assays and displayed figures are representative.

Supplementary Material

Refer to Web version on PubMed Central for supplementary material.

Acknowledgments

This work was supported by the intramural research programs of the *Eunice Kennedy Shriver* National Institute of Child Health and Human Development and the National Human Genome Research Institute, a pilot award for iPSC research from the National Institutes of Health Center for Regenerative Medicine, and National Institutes of Health grant GM110128 (W.C.). We thank Kayla Perez, Nicole Khezri, and Gian Franco Rodriguez for assistance with hESC and iPSC culture. We also thank Cynthia Toth and Alexa Ely for assistance with mice and sequencing. We thank Amalia Dutra, Evgenia Pak, and the NHGRI Cytogenetics Core for assistance with hESC/iPSC karyotyping. We thank Louis (Chip) Dye and the NICHD Microscopy and Imaging Core for electron microscopy assistance. We thank Dr. Barbara S. Mallon (NINDS), Dr. Sergei Kuznetsov (NIDCR), and Dr. Pamela G. Robey (NIDCR) for experimental advice and the i19 and i21 hiPSC lines. We thank Dr. Jason Mills (Children's Hospital of Philadelphia) for experimental advice, the NHLBI iPS Core Facility for assistance with Lathosterolosis iPSC generation, and Dr. Mahendra Rao and Dr. Karl Pfeifer for critical discussions. Finally, we would like to thank the patients and guardians who participated in the NIH clinical program and contributed to this study.

References

1. Porter FD, Herman GE. Malformation syndromes caused by disorders of cholesterol synthesis. J Lipid Res. 2011; 52:6–34. DOI: 10.1194/jlr.R009548 [PubMed: 20929975]
2. Wassif CA, et al. Mutations in the human sterol delta7-reductase gene at 11q12-13 cause Smith-Lemli-Opitz syndrome. Am J Hum Genet. 1998; 63:55–62. S0002-9297(07)60776-9 [pii]. DOI: 10.1086/301936 [PubMed: 9634533]
3. Spector AA, Yorek MA. Membrane lipid composition and cellular function. J Lipid Res. 1985; 26:1015–1035. [PubMed: 3906008]
4. Lingwood D, Simons K. Lipid rafts as a membrane-organizing principle. Science. 2010; 327:46–50. DOI: 10.1126/science.1174621 [PubMed: 20044567]
5. Jurevics H, Morell P. Cholesterol for synthesis of myelin is made locally, not imported into brain. Journal of neurochemistry. 1995; 64:895–901. [PubMed: 7830084]
6. Mellon SH. Neurosteroid regulation of central nervous system development. Pharmacology & therapeutics. 2007; 116:107–124. DOI: 10.1016/j.pharmthera.2007.04.011 [PubMed: 17651807]
7. Lee RW, Conley SK, Gropman A, Porter FD, Baker EH. Brain magnetic resonance imaging findings in Smith-Lemli-Opitz syndrome. Am J Med Genet A. 2013; 161:2407–2419. DOI: 10.1002/ajmg.a.36096 [PubMed: 23918729]
8. Tierney E, et al. Behavior phenotype in the RSH/Smith-Lemli-Opitz syndrome. Am J Med Genet. 2001; 98:191–200. pii. DOI: 10.1002/1096-8628(20010115)98:2<191::AID-AJMG1030>3.0.CO;2-M [PubMed: 11223857]
9. Gaoua W, Chevy F, Roux C, Wolf C. Oxidized derivatives of 7-dehydrocholesterol induce growth retardation in cultured rat embryos: a model for antenatal growth retardation in the Smith-Lemli-Opitz syndrome. J Lipid Res. 1999; 40:456–463. [PubMed: 10064734]
10. Xu L, Korade Z, Rosado DA Jr, Mirnics K, Porter NA. Metabolism of oxysterols derived from nonenzymatic oxidation of 7-dehydrocholesterol in cells. J Lipid Res. 2013; 54:1135–1143. DOI: 10.1194/jlr.M035733 [PubMed: 23381570]
11. Somers A, et al. Generation of transgene-free lung disease-specific human induced pluripotent stem cells using a single excisable lentiviral stem cell cassette. Stem Cells. 2010; 28:1728–1740. DOI: 10.1002/stem.495 [PubMed: 20715179]

12. Hu BY, et al. Neural differentiation of human induced pluripotent stem cells follows developmental principles but with variable potency. Proc Natl Acad Sci U S A. 2010; 107:4335–4340. 0910012107 [pii]. DOI: 10.1073/pnas.0910012107 [PubMed: 20160098]
13. Ludwig TE, et al. Derivation of human embryonic stem cells in defined conditions. Nat Biotechnol. 2006; 24:185–187. DOI: 10.1038/nbt1177 [PubMed: 16388305]
14. Jiang XS, et al. Activation of Rho GTPases in Smith-Lemli-Opitz syndrome: pathophysiological and clinical implications. Hum Mol Genet. 2010; 19:1347–1357. ddq011 [pii]. DOI: 10.1093/hmg/ddq011 [PubMed: 20067919]
15. Elkabetz Y, et al. Human ES cell-derived neural rosettes reveal a functionally distinct early neural stem cell stage. Genes Dev. 2008; 22:152–165. 22/2/152 [pii]. DOI: 10.1101/gad.1616208 [PubMed: 18198334]
16. Cenedella RJ, Bierkamper GG. Mechanism of cataract production by 3-beta(2-diethylaminoethoxy) androst-5-en-17-one hydrochloride, U18666A: an inhibitor of cholesterol biosynthesis. Experimental eye research. 1979; 28:673–688. [PubMed: 467524]
17. Gofflot F, Kolf-Clauw M, Clotman F, Roux C, Picard JJ. Absence of ventral cell populations in the developing brain in a rat model of the Smith-Lemli-Opitz syndrome. Am J Med Genet. 1999; 87:207–216. pii. DOI: 10.1002/(SICI)1096-8628(19991126)87:3<207::AID-AJMG3>3.0.CO;2-5 [PubMed: 10564872]
18. Frolov A, et al. Cholesterol overload promotes morphogenesis of a Niemann-Pick C (NPC)-like compartment independent of inhibition of NPC1 or HE1/NPC2 function. J Biol Chem. 2001; 276:46414–46421. DOI: 10.1074/jbc.M108099200 [PubMed: 11571306]
19. Wassif CA, et al. Cholesterol storage defect in RSH/Smith-Lemli-Opitz syndrome fibroblasts. Mol Genet Metab. 2002; 75:325–334. DOI: 10.1016/S1096-7192(02)00010-0 [PubMed: 12051964]
20. Krakowiak PA, et al. Lathosterolosis: an inborn error of human and murine cholesterol synthesis due to lathosterol 5-desaturase deficiency. Hum Mol Genet. 2003; 12:1631–1641. [PubMed: 12812989]
21. Sato N, Meijer L, Skaltsounis L, Greengard P, Brivanlou AH. Maintenance of pluripotency in human and mouse embryonic stem cells through activation of Wnt signaling by a pharmacological GSK-3-specific inhibitor. Nature medicine. 2004; 10:55–63. DOI: 10.1038/nm979
22. Fernandez A, et al. The WNT receptor FZD7 is required for maintenance of the pluripotent state in human embryonic stem cells. Proc Natl Acad Sci U S A. 2014; 111:1409–1414. DOI: 10.1073/pnas.1323697111 [PubMed: 24474766]
23. Lie DC, et al. Wnt signalling regulates adult hippocampal neurogenesis. Nature. 2005; 437:1370–1375. DOI: 10.1038/nature04108 [PubMed: 16251967]
24. Hirabayashi Y, et al. The Wnt/beta-catenin pathway directs neuronal differentiation of cortical neural precursor cells. Development. 2004; 131:2791–2801. DOI: 10.1242/dev.01165 [PubMed: 15142975]
25. Blauwkamp TA, Nigam S, Ardehali R, Weissman IL, Nusse R. Endogenous Wnt signalling in human embryonic stem cells generates an equilibrium of distinct lineage-specified progenitors. Nature communications. 2012; 3:1070.
26. Sheng R, et al. Cholesterol selectively activates canonical Wnt signalling over non-canonical Wnt signalling. Nature communications. 2014; 5:4393.
27. Sheng R, et al. Cholesterol modulates cell signaling and protein networking by specifically interacting with PDZ domain-containing scaffold proteins. Nature communications. 2012; 3:1249.
28. Buchovecky CM, et al. A suppressor screen in Mecp2 mutant mice implicates cholesterol metabolism in Rett syndrome. Nature genetics. 2013; 45:1013–1020. DOI: 10.1038/ng.2714 [PubMed: 23892605]
29. Munji RN, Choe Y, Li G, Siegenthaler JA, Pleasure SJ. Wnt signaling regulates neuronal differentiation of cortical intermediate progenitors. J Neurosci. 2011; 31:1676–1687. DOI: 10.1523/JNEUROSCI.5404-10.2011 [PubMed: 21289176]
30. Chenn A, Walsh CA. Regulation of cerebral cortical size by control of cell cycle exit in neural precursors. Science. 2002; 297:365–369. DOI: 10.1126/science.1074192 [PubMed: 12130776]

31. Mutch CA, Schulte JD, Olson E, Chenn A. Beta-catenin signaling negatively regulates intermediate progenitor population numbers in the developing cortex. PLoS One. 2010; 5:e12376. [PubMed: 20811503]
32. Inestrosa NC, Arenas E. Emerging roles of Wnts in the adult nervous system. Nat Rev Neurosci. 2010; 11:77–86. DOI: 10.1038/nrn2755 [PubMed: 20010950]
33. Sowers LP, et al. Disruption of the non-canonical Wnt gene PRICKLE2 leads to autism-like behaviors with evidence for hippocampal synaptic dysfunction. Molecular psychiatry. 2013; 18:1077–1089. DOI: 10.1038/mp.2013.71 [PubMed: 23711981]
34. Mohn JL, et al. Adenomatous polyposis coli protein deletion leads to cognitive and autism-like disabilities. Molecular psychiatry. 2014
35. Mermelstein CS, Portilho DM, Mendes FA, Costa ML, Abreu JG. Wnt/beta-catenin pathway activation and myogenic differentiation are induced by cholesterol depletion. Differentiation; research in biological diversity. 2007; 75:184–192. DOI: 10.1111/j.1432-0436.2006.00129.x
36. Yamaguchi TP, Bradley A, McMahon AP, Jones S. A Wnt5a pathway underlies outgrowth of multiple structures in the vertebrate embryo. Development. 1999; 126:1211–1223. [PubMed: 10021340]
37. Amar MJ, et al. 5A apolipoprotein mimetic peptide promotes cholesterol efflux and reduces atherosclerosis in mice. The Journal of pharmacology and experimental therapeutics. 2010; 334:634–641. DOI: 10.1124/jpet.110.167890 [PubMed: 20484557]
38. Lowry WE, et al. Generation of human induced pluripotent stem cells from dermal fibroblasts. Proc Natl Acad Sci U S A. 2008; 105:2883–2888. DOI: 10.1073/pnas.0711983105 [PubMed: 18287077]
39. Krakowiak PA, et al. Mutation analysis and description of sixteen RSH/Smith-Lemli-Opitz syndrome patients: polymerase chain reaction-based assays to simplify genotyping. Am J Med Genet. 2000; 94:214–227. [PubMed: 10995508]
40. Davisson MT, Akeson EC. An improved method for preparing G-banded chromosomes from mouse peripheral blood. Cytogenetics and cell genetics. 1987; 45:70–74. [PubMed: 3622012]
41. Cong L, et al. Multiplex genome engineering using CRISPR/Cas systems. Science. 2013; 339:819–823. DOI: 10.1126/science.1231143 [PubMed: 23287718]
42. Ran FA, et al. Genome engineering using the CRISPR-Cas9 system. Nat Protoc. 2013; 8:2281–2308. DOI: 10.1038/nprot.2013.143 [PubMed: 24157548]
43. Xue W, et al. CRISPR-mediated direct mutation of cancer genes in the mouse liver. Nature. 2014; 514:380–384. DOI: 10.1038/nature13589 [PubMed: 25119044]
44. Stahelin RV, Cho W. Differential roles of ionic, aliphatic, and aromatic residues in membrane-protein interactions: a surface plasmon resonance study on phospholipases A2. Biochemistry. 2001; 40:4672–4678. [PubMed: 11294634]
45. Stahelin RV, Cho W. Roles of calcium ions in the membrane binding of C2 domains. Biochem J. 2001; 359:679–685. [PubMed: 11672443]
46. Ananthanarayanan B, Stahelin RV, Digman MA, Cho W. Activation mechanisms of conventional protein kinase C isoforms are determined by the ligand affinity and conformational flexibility of their C1 domains. J Biol Chem. 2003; 278:46886–46894. DOI: 10.1074/jbc.M307853200 [PubMed: 12954613]
47. Cho W, Bittova L, Stahelin RV. Membrane binding assays for peripheral proteins. Anal Biochem. 2001; 296:153–161. DOI: 10.1006/abio.2001.5225 [PubMed: 11554709]
48. Hsieh JC, et al. Mesd encodes an LRP5/6 chaperone essential for specification of mouse embryonic polarity. Cell. 2003; 112:355–367. [PubMed: 12581525]
49. Koyama-Honda I, et al. Fluorescence imaging for monitoring the colocalization of two single molecules in living cells. Biophys J. 2005; 88:2126–2136. DOI: 10.1529/biophysj.104.048967 [PubMed: 15596511]
50. Zidovetzki R, Levitan I. Use of cyclodextrins to manipulate plasma membrane cholesterol content: evidence, misconceptions and control strategies. Biochim Biophys Acta. 2007; 1768:1311–1324. DOI: 10.1016/j.bbamem.2007.03.026 [PubMed: 17493580]

51. Wassif CA, et al. Biochemical, phenotypic and neurophysiological characterization of a genetic mouse model of RSH/Smith--Lemli--Opitz syndrome. Hum Mol Genet. 2001; 10:555–564. [PubMed: 11230174]

52. Ahn S, Joyner AL. In vivo analysis of quiescent adult neural stem cells responding to Sonic hedgehog. Nature. 2005; 437:894–897. DOI: 10.1038/nature03994 [PubMed: 16208373]

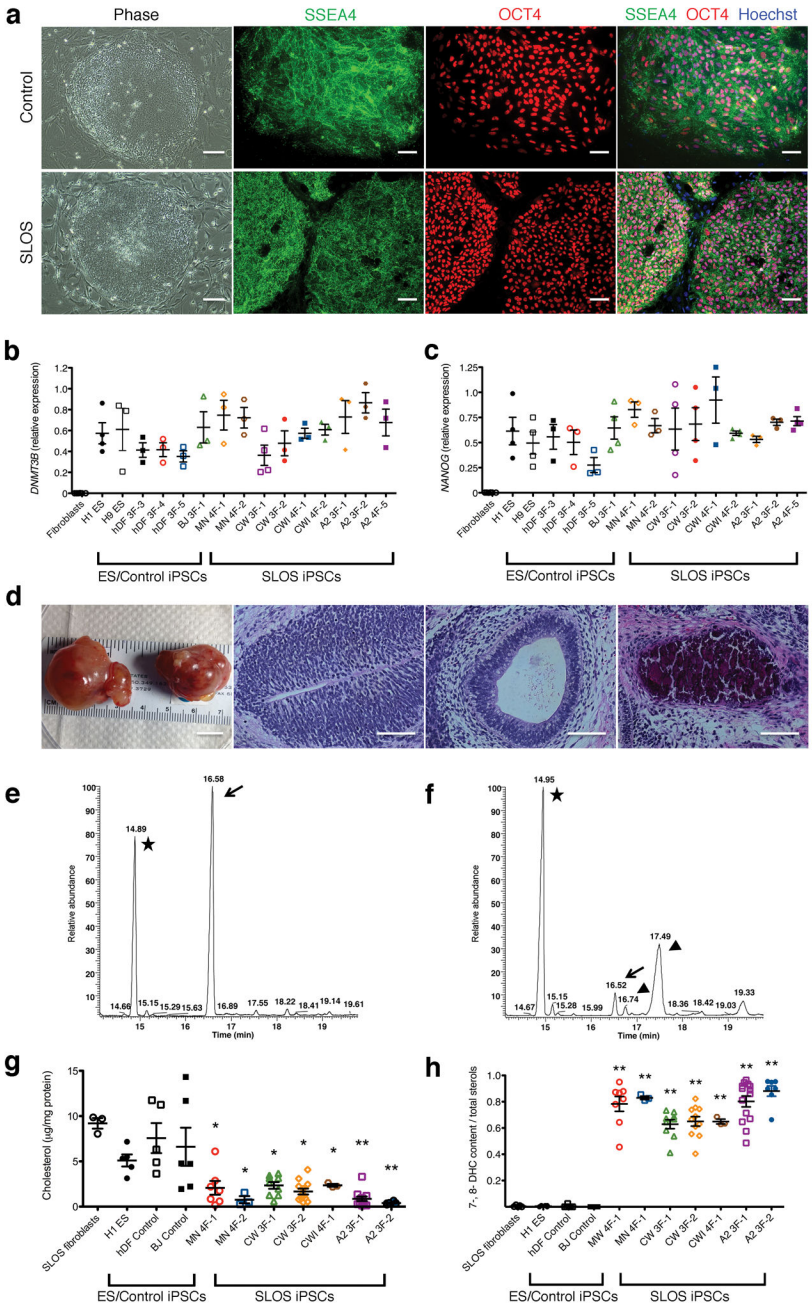

Figure 1. Generation of iPSCs from Smith-Lemli-Opitz syndrome subjects

(**a**) Example immunocytochemistry images depicting expression of pluripotency markers SSEA4 and OCT4 in control (line BJ 3F-1) and SLOS (line A2 3F-2) iPSCs. Scale bars, 200 µm in phase contrast images and 100 µm in fluorescence images. (**b–c**) Quantification of relative *DNMT3B* and *NANOG* transcript expression in SLOS fibroblasts, hESCs, control iPSCs, and SLOS iPSCs. $n = 3$ for all cell lines except H1, CW 3F-1 (*DNMT3B*, $n = 4$) and H1, H9, BJ 3F-1, CW 3F-1, CW 3F-2, CWI 4F-2, A2 4F-5 (*NANOG*, $n = 4$); data represent mean ± s.e.m. (**d**) Example images of gross and stained (hematoxylin and eosin) teratomas obtained 4–8 weeks after injection of SLOS iPSCs into NOD/SCID immunocompromised

mice. Stained panels, from left to right, depict the formation of neuroectoderm, glandular endothelium, and bone. Scale bars, 1 cm (left panel) and 100 μm (remaining panels). Representative images from three injected mice for BJ 3F-1 control and A2 3F-2 SLOS iPSCs are shown. (**e–f**) Example gas chromatography/mass spectrometric analysis of extracted lipids from control (**e**) and SLOS (**f**) iPSCs cultured in cholesterol deficient mTesR1 media for 7 days. Stars at 14.8 – 15.0 min peaks indicate the internal standard coprostanol; Arrows at 16.5 – 16.6 min peaks indicate cholesterol. Arrowheads in (**f**) at 16.74 min and 17.49 min indicate 8DHC and 7DHC, respectively. (**g–h**) Quantification of cholesterol (**g**) and DHC (**h**) levels for SLOS fibroblasts cultured in cholesterol replete media and hESCs, control iPSCs, and SLOS iPSCs cultured for 3 – 7 d in cholesterol deficient mTesR1 media. SLOS fibroblasts in cholesterol replete medium n = 5, H1 ES n = 6, hDF control n = 7, BJ control n = 5, MN 4F-1 n = 8, MN 4F-2 n = 3, CW 3F-1 n = 9, CW 3F-2 n = 11, CWI 4F-1 n = 3, A2 3F-1 n = 14, A2 3F-2 n = 7 per cell line; unpaired, two-tailed student's *t* test against H1 ES cells; data represent mean ± s.e.m. * $P < 0.05$ and ** $P < 0.01$.

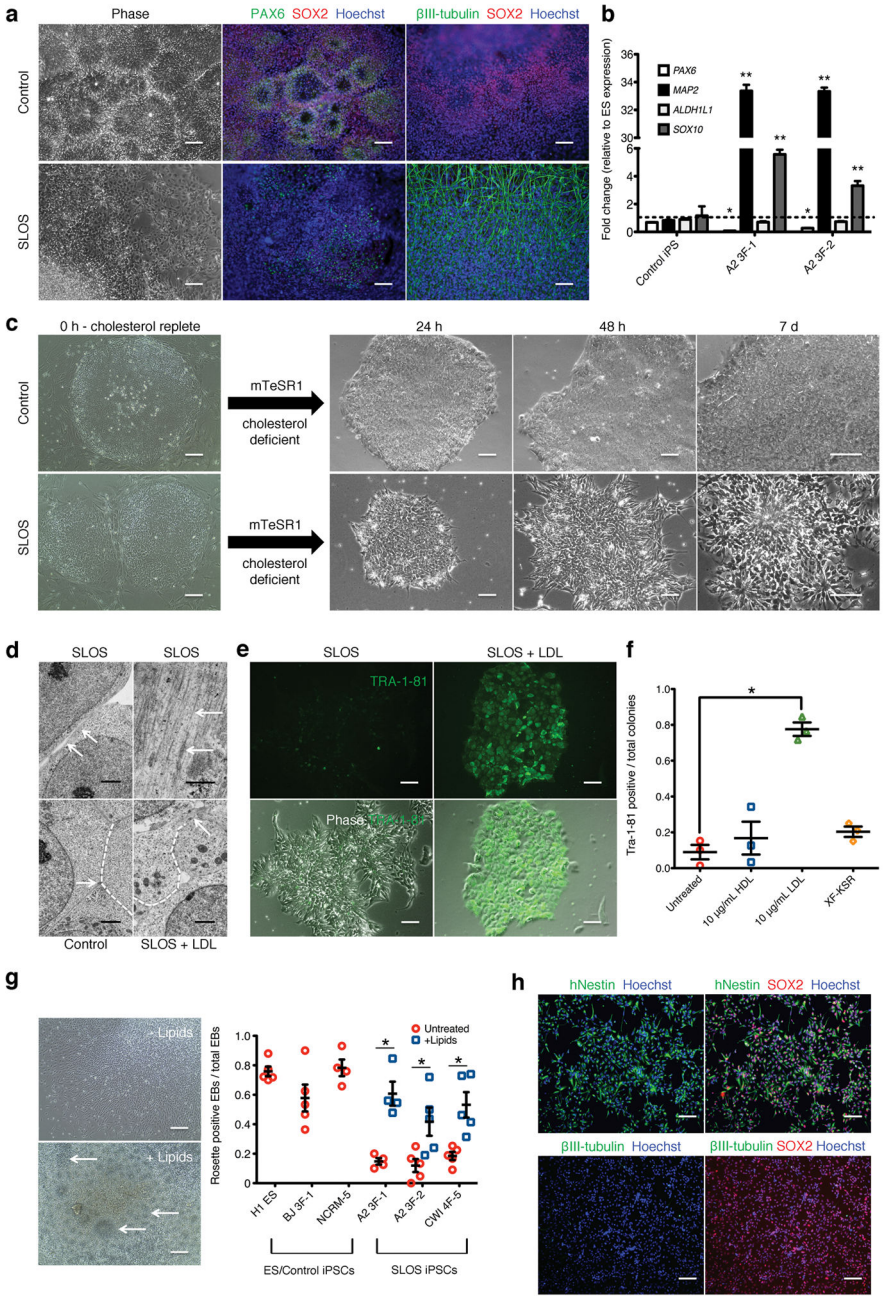

Figure 2. SLOS iPSCs exhibit accelerated neural differentiation and loss of pluripotency in cholesterol deficient conditions

(**a**) Representative neural rosette formation in controls (line H1 ES) and SLOS iPSCs (line A2 3F-1). PAX6 (green) and SOX2 (red) label neural rosettes; βIII-tubulin (green) labels neurons. Hoechst is blue; scale bars, 100 μm. (**b**) Quantification of relative transcript expression of lineage markers *PAX6* (neural progenitors), *MAP2* (neuronal), *SOX10* (neural crest), and *ALDHL1* (glial) in rosette formation assays in control and SLOS (lines A2 3F-1, A2 3F-2) iPSCs. n = 3 biological replicates per cell line; unpaired, two-tailed student's *t* test compared to H1 ES cell expression (dashed line); data represent mean ± s.e.m. (**c**)

Representative images of control (top panels, line BJ 3F-1) and SLOS (bottom panels, line A2 3F-2) iPSCs cultured in cholesterol replete (0 h) versus cholesterol deficient (24 h, 48 h, and 7 d) conditions; scale bars, 200 μm. Representative images from n = 10 biological replicates. (**d**) Electron microscopic analysis of controls (line H1 ES) and SLOS iPSCs (line A2 3F-1) in cholesterol deficient conditions. Loss of gap and tight junctions (arrows, top left panel) and formation of intermediate filaments (arrows, top right panel) are indicated. Controls (bottom left panel) and LDL supplemented SLOS iPSCs (bottom right panel) maintain gap and tight junctions (arrows, bottom panels; dashed lines identify cell-cell border maintenance); top right scale bar, 0.5 μm, other scale bars, 2 μm. H1 ES n = 10 cells, A2 3F-1 n = 12 cells, A2 3F-1+LDL n = 21 cells. Representative images are shown. (**e**) Pluripotent TRA-1-81 expression and phase contrast images of SLOS iPSCs (line A2 3F-1) cultured in cholesterol deficient (left panels) or LDL supplemented (right panels) conditions; scale bars, 100 μm. (**f**) Quantitation of TRA-1-81^{+} SLOS iPSC (line A2 3F-1) colonies cultured in cholesterol deficient mTeSR1 (untreated), mTeSR1 + LDL (10 mcg/mL medium), mTeSR1 + HDL (10 mcg/mL medium), or XF-KSR medium (1.85 mcg cholesterol/mL medium). n = 3 biological replicates per treatment, 250 – 300 colonies per replicate; unpaired, two-tailed student's *t* test compared to untreated; data represent mean ± s.e.m. (**g**) Representative images of rosette formation by SLOS iPSCs (line A2 3F-2) with or without lipid supplementation (left panels); scale bars, 100 μm. Quantitation of rosette formation with or without lipid supplementation. H1 ES n = 5, BJ 3F-1 n = 5, NL5 n = 4, A2 3F-1 n = 4, A2 3F-2 n = 5, CWI 4F-5 n = 5 biological replicates; unpaired, two-tailed student's *t* test compared to untreated; data represent mean ± s.e.m. (**h**) Neural progenitor (SOX2, red; hNESTIN, green) and neuronal (βIII-tubulin, green) marker expression in expandable SLOS neural progenitors; Hoechst is blue; scale bars, 100 μm. Representative images from n = 3 biological replicates for A2 3F-2 are shown. * $P < 0.05$; ** $P < 0.01$.

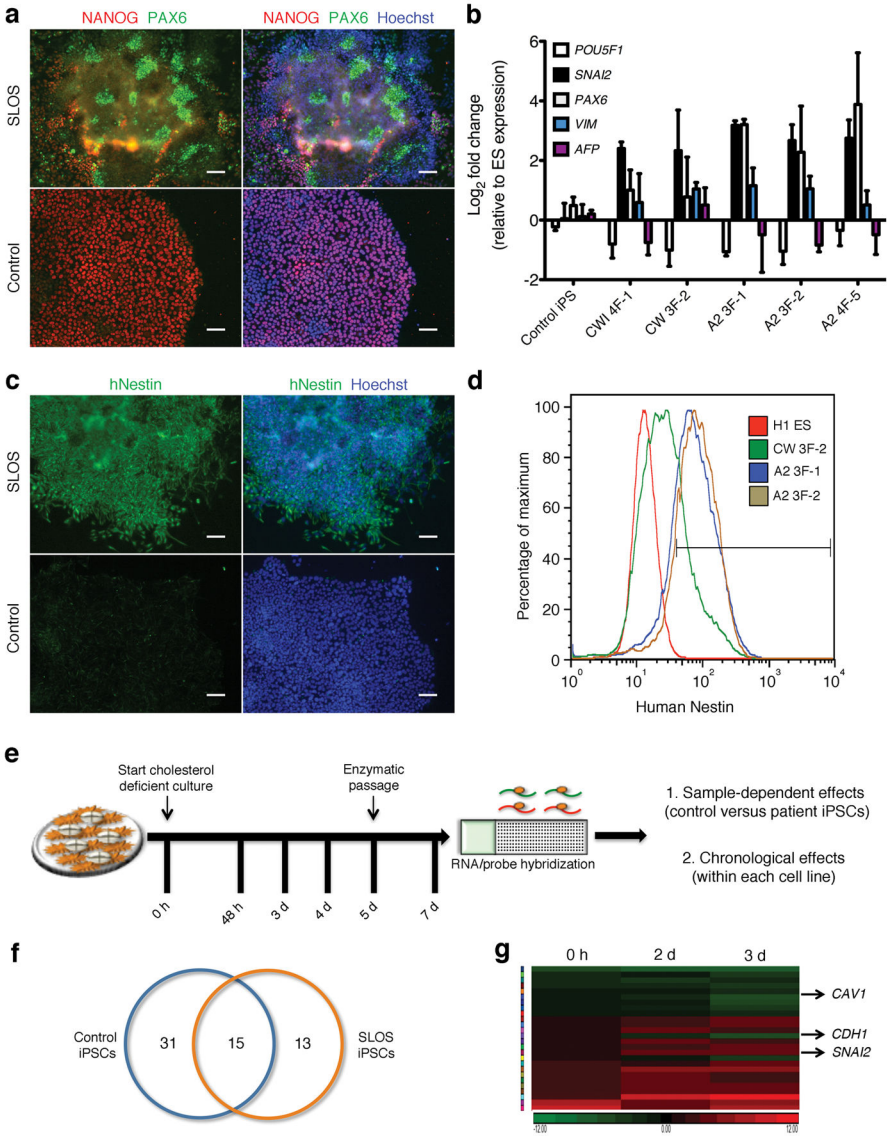

Figure 3. Loss of normal DHCR7 activity induces epithelial-mesenchymal transition and neural differentiation of iPSCs through discreet signaling pathways

(**a**) Representative images of pluripotent (NANOG, red) and neural progenitor (PAX6, green) marker expression in SLOS (line A2 3F-1) and control (line BJ 3F-1) iPSCs cultured in mTeSR1 cholesterol deficient pluripotent media. Hoechst is blue; scale bars, 100 μm. (**b**) Quantification of *POU5F1* (pluripotent), *PAX6* (neuroectoderm), *SNAI2* (neural crest), *VIM* (mesoderm/mesenchymal) and *AFP* (endoderm) transcript expression in control (line BJ 3F-1) and SLOS iPSCs cultured in cholesterol deficient pluripotent conditions. CWI 4F-1, CW 3F-2 n = 4, Control iPS, A2 3F-1, A2 3F-2, A2 4F-5 n = 3 biological replicates compared to H1 ES n = 3; data represent mean ± s.e.m. (**c**) hNestin (green) expression in SLOS iPSCs (line A2 3F-1) and controls (line H1 ES) after 7 d cholesterol deficient culture. Hoechst is blue; scale bars, 100 μm. (**d**) FACS quantitation of hNestin in SLOS iPSCs (lines CW 3F-2, A2 3F-1, A2 3F-2) and H1 ES cells after 7 d cholesterol deficient culture. Representative data from n = 3 biological replicates is shown. (**e**) Schematic representation

of a microarray experiment to compare expression patterns in control (line BJ 3F-1) and SLOS (line A2 3F-2) iPSCs grown in cholesterol deficient conditions. n = 4 biological replicates were collected and analyzed at all time points. **(f)** Venn diagram highlights the number of genes differentially expressed between control and SLOS iPSCs on Days 2 and 3 of cholesterol deficient culture. (**g**) Heat map shows the relative intensity for selected statistically significant genes at the indicated time points.

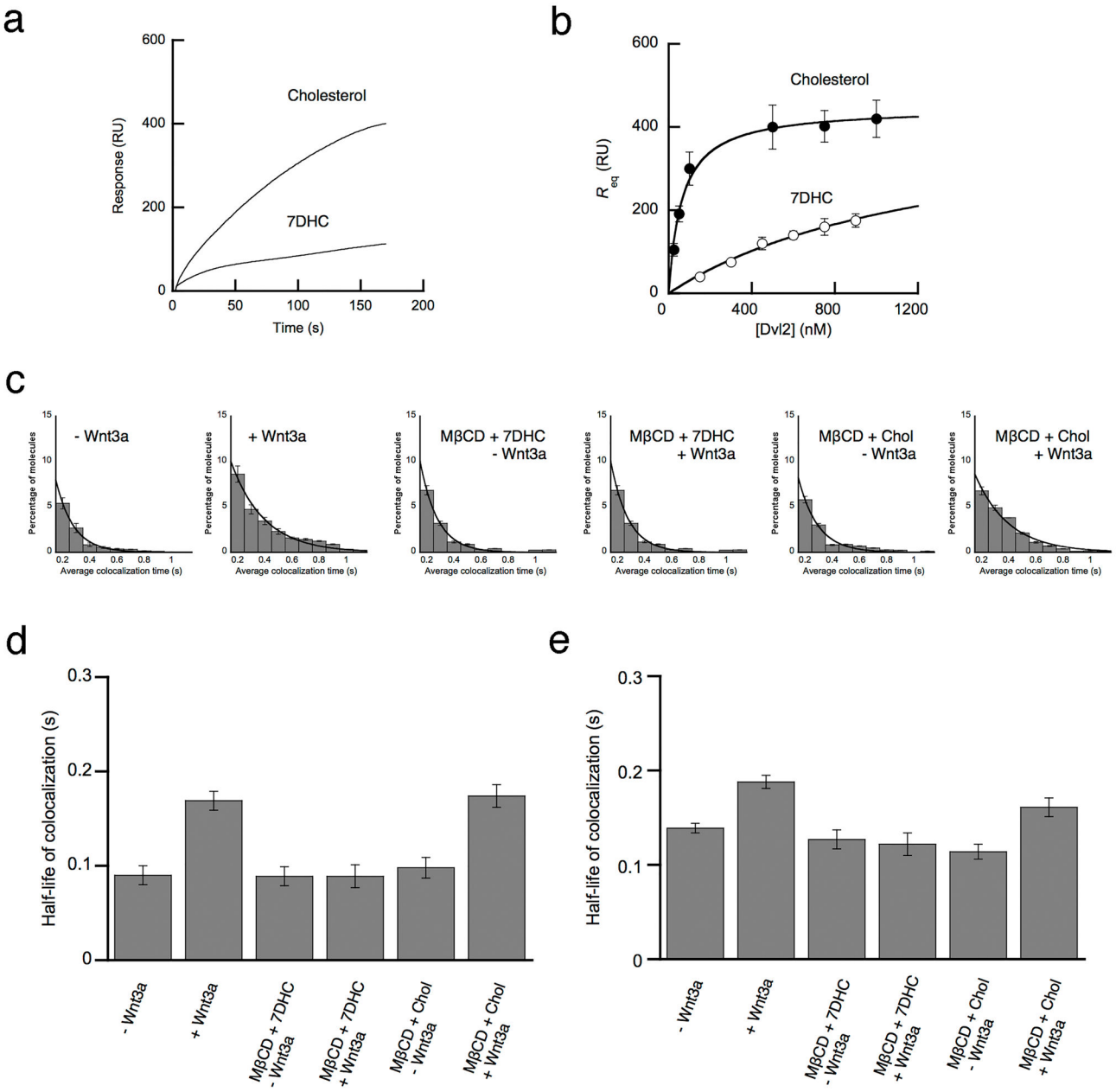

Figure 4. 7-dehydrocholesterol accumulation inhibits binding between canonical Wnt signaling proteins

(**a**) Sensorgrams of DVL2-PDZ binding to PM-mimetic vesicles containing cholesterol (Chol) or 7-dehydroxycholesterol (7DHC) obtained by kinetic SPR analysis. [DVL2-PDZ] = 500 nM. n = 3 biological replicates. (**b**) Determination of K_d for DVL2-PDZ-vesicle binding by equilibrium SPR analysis. The binding isotherms were generated from the R_{eq} versus the concentration (P_0) of Dvl2-PDZ plots. Solid lines represent theoretical curves constructed from R_{max} and K_d values determined by nonlinear least squares analysis of the isotherm using the following equation: $R_{eq} = R_{max}/(1 + K_d/P_0)$. K_d = 60 ± 20 nM for Chol-containing PM vesicles and 1,300 ± 200 nM for 7DHC-containing PM vesicles, respectively. n = 3

biological replicates. (**c**) Dynamic colocalization of EGFP-tagged DVL2 and Halo-TMR-labeled FZ7 in HeLa cells upon Wnt3a stimulation. Histograms display percentages of DVL2 molecules spending a given colocalization time (> 0.2 s) with FZ7 on the plasma membrane of HeLa cells. n = 3 biological replicates. (**d**) The effect of 7DHC on the half-life of colocalization for DVL2 and FZ7. n = 3 biological replicates; data represent mean ± s.d. (**e**) The effect of 7DHC on the half-life of colocalization for LRP6 and FZ7. The half-life of co-localization was calculated from the dissociation rate constant (k), which was determined by non-linear least-squares analysis of histograms using a single-exponential decay equation (i.e., $P = P_O\, e^{-kt}$). The same PM surface size was analyzed for each histogram. n = 3 biological replicates; data represent mean ± s.d. 50 ng/mL Wnt3a was used in all experiments.

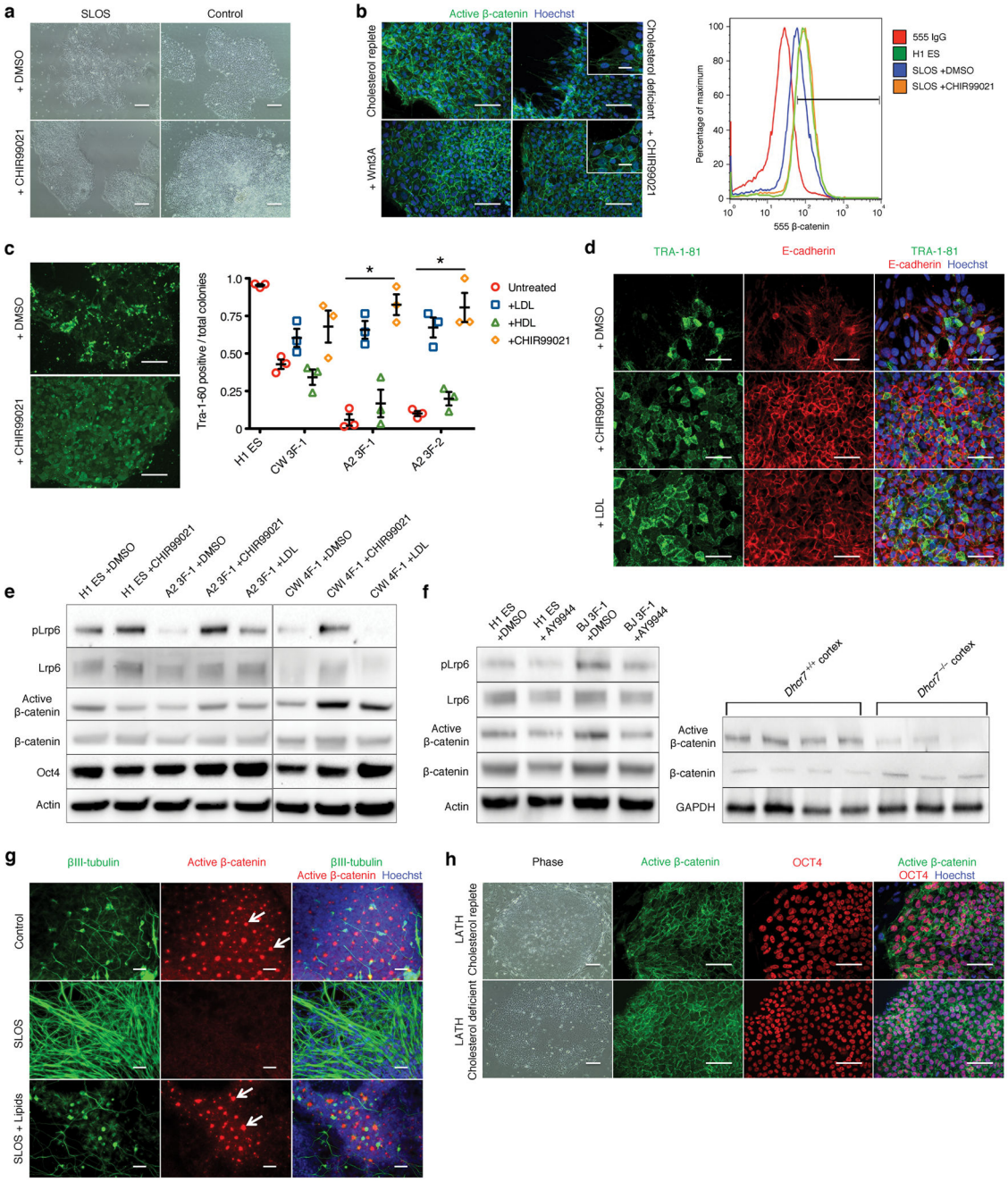

Figure 5. *DHCR7* mutation induces loss of functional β-catenin and causes human stem cell differentiation

(**a**) Representative images of controls (line H1 ES) and SLOS iPSCs (line A2 3F-1) in cholesterol deficient conditions treated with DMSO or the GSK3β inhibitor CHIR99021; scale bars, 200 μm. (**b**) Representative expression of active β-catenin (green) in SLOS iPSCs (line A2 3F-2) cultured under cholesterol replete or cholesterol deficient conditions (top panels) for 3 d, as well as recombinant Wnt3A or CHIR99021 supplementation to cholesterol deficient conditions (bottom panels). Hoechst is blue; scale bars, 100 μm. FACS analysis of β-catenin expression in controls (line H1 ES) and SLOS iPSCs (line A2 3F-2),

with or without CHIR99021 treatment. n = 3 biological replicates per treatment. (**c**) Representative images of TRA-1-60 expression in SLOS iPSCs (line A2 3F-2) with DMSO or CHIR99021 treatment. Quantitation of TRA-1-60^{+} colonies in control (line H1 ES) and SLOS iPSCs (lines CW 3F-1, A2 3F-1, A2 3F-2) cultured in cholesterol deficient conditions for 3 d; scale bars, 100 μm. n = 3 biological replicates; unpaired, two-tailed student's *t* test compared to untreated; data represent mean ± s.e.m. (**d**) Representative images of TRA-1-81 (green) and E-cadherin (red) in SLOS iPSCs (line A2 3F-2) cultured in cholesterol deficient conditions for 3 d with DMSO, CHIR99021, or LDL. Hoechst is blue; scale bars, 100 μm. (**e**) Western blot analysis of H1 ES cells and SLOS iPSCs (lines A2 3F-1, CWI 4F-1) cultured in cholesterol deficient conditions for 4 d, while treated with DMSO, CHIR99021, or LDL. Blots were probed for β-catenin, active β-catenin, OCT4, LRP6, and pLRP6. Actin was utilized as a loading control. Representative Western blot of n = 3 biological replicates for all samples except CWI 4F-1, pLRP6, n = 2). (**f**) Western blots of DMSO or AY9944 treated 4 d control rosette assays (lines H1 ES, BJ 3F-1) and the cerebral cortex of *Dhcr7*$^{-/-}$ mice. Blots were probed for LRP6 and pLRP6 (AY9944 treated) or β-catenin and active β-catenin (cortex and AY9944 treated). Actin was utilized as a loading control for rosette assays and GAPDH for brain tissue. Representative Western blots are shown. n = 3 for AY9944 treatments; n = 7 for *Dhcr7*$^{+/-}$, *Dhcr7*$^{-/-}$ cortex; n = 3 for *Dhcr7*$^{+/-}$ cortex. (**g**) Images of 4 d rosette formation assays in control (line H1 ES) and SLOS iPSCs (line A2 3F-2, with and without lipid supplementation) demonstrating expression of active β-catenin (red) and βIII-tubulin expression (green). Hoechst is blue; scale bars, 100 μm. (**h**) Representative images of pluripotent morphology and expression of active β-catenin (green) and OCT4 (red) in Lathosterolosis iPSCs (line LATH 4F-1) within cholesterol replete and cholesterol deficient conditions. Hoechst is blue; scale bar, 200 μm (in phase) and 100 μm (in fluorescent). * $P < 0.05$.

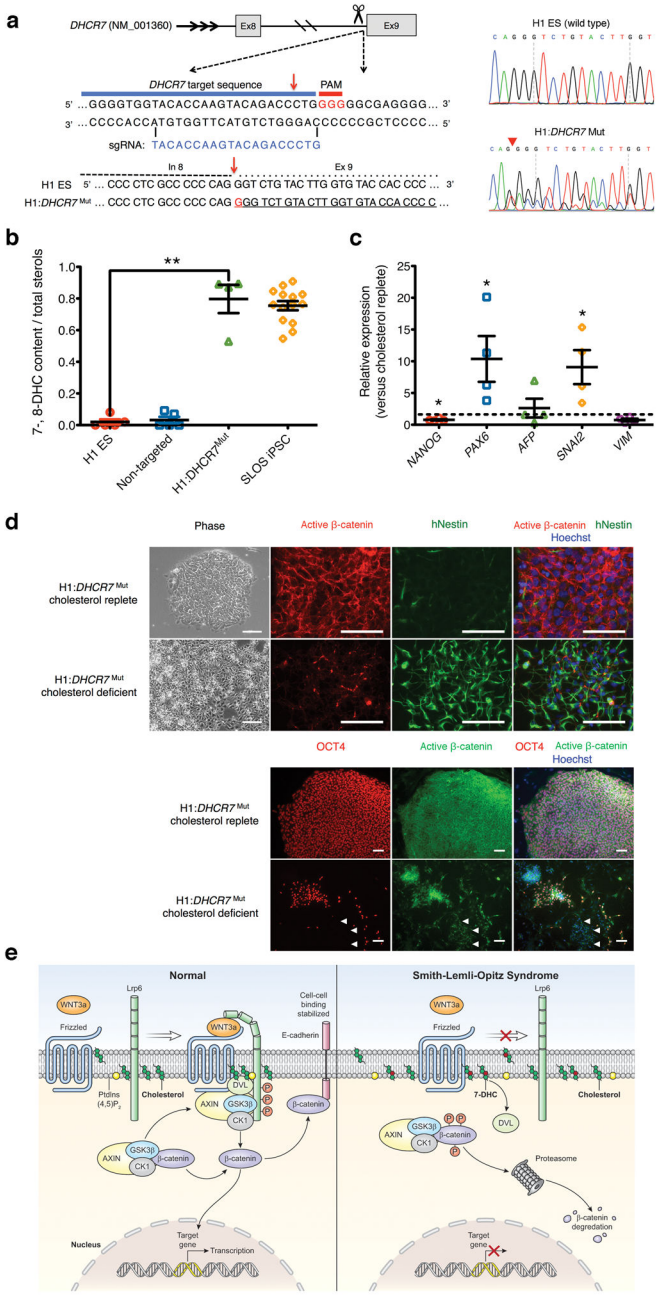

Figure 6. H1:*DHCR7*^{Mut} ESCs display SLOS biochemical defects, differentiation defects, and loss of β-catenin activity

(**a**) Schematic illustrating CRISPR/Cas9 targeting of *DHCR7* and insertion event in H1:*DHCR7*^{Mut}. Red arrowhead in H1:*DHCR7*^{Mut} chromatogram indicates location of Cas9 nuclease activity. (**b**) GC/MS quantitation of 7DHC and 8DHC in H1:*DHCR7*^{Mut} iPSCs, SLOS iPSCs, H1 ES, and non-targeted H1 ES. H1 ES n = 5, Non-targeted n = 5, H1:*DHCR7*^{Mut} n = 4, SLOS iPSC n = 14 biological replicates; unpaired, two-tailed student's *t* test; data represent mean ± s.e.m. (**c**) qRT-PCR analysis of *NANOG* (pluripotency), *PAX6* (neuroectoderm), *SNAI2* (neural crest), *AFP* (endoderm), or *VIM*

(mesoderm). n = 4 biological replicates; data represent mean ± s.e.m.; unpaired, two-tailed student's *t* test compared to untreated. (**d**) Representative images of active β-catenin and hNestin in H1:*DHCR7*^{Mut} cells in cholesterol replete (top panels) and after 14 d cholesterol deficient culture (bottom panels). Representative areas of differentiation indicated by loss of OCT4 and active β-catenin are designated with white arrowheads. Hoechst is blue; scale bars, 100 μm. (**e**) Model for the effects of DHC accumulation on Wnt/β-catenin signaling. DHC buildup and cholesterol loss limits formation of the DVL/LRP/FRIZZLED receptor complex, allowing GSK3β-mediated degradation of β-catenin and resulting in aberrant differentiation. * $P < 0.05$; ** $P < 0.01$.